# **CONFERENCE PRE-PRINT**

# ADVANCES IN PHYSICS AND APPLICATIONS OF 3D MAGNETIC PERTURBATIONS ON THE J-TEXT TOKAMAK

Nengchao Wang<sup>1</sup>, Yonghua Ding<sup>1</sup>, Zhongyong Chen<sup>1</sup>, Donghui Xia<sup>1</sup>, Zhoujun Yang<sup>1</sup>, Zhipeng Chen<sup>1</sup>, Wei Zheng<sup>1</sup>, Wei Yan<sup>1</sup>, Da Li<sup>2</sup>, Song Zhou<sup>1</sup>, Chengshuo Sheng<sup>1</sup>, Zhengkang Ren<sup>1</sup>, Feiyue Mao<sup>1</sup>, Yangbo Li<sup>1</sup>, Xixuan Chen<sup>1</sup>, Chuanxu Zhao<sup>1</sup>, Qinghu Yang<sup>1</sup>, Qinlin Tao<sup>1</sup>, Wentao Geng<sup>1</sup>, Hanhui Li<sup>3</sup>, Jie Yang<sup>1</sup>, Jiankun Hua<sup>1</sup>, Xinku Ai<sup>1</sup>, Xin Xu<sup>1</sup>, Junli Zhang<sup>1,3</sup>, Zhangrong Hou<sup>1</sup>, Jiangang Fang<sup>1</sup>, Chi Lei<sup>1</sup>, Fengming Xue<sup>1</sup>, Xinkun Ai<sup>1</sup>, Yu Zhong<sup>1</sup>, Ting Long<sup>2</sup>, Zhonghe Jiang<sup>1</sup>, Li Gao<sup>1</sup>, Xiaoqing Zhang<sup>1</sup>, Bo Rao<sup>1</sup>, Zhifeng Cheng<sup>4</sup>, Lu Wang<sup>1</sup>, Weixin Guo<sup>1</sup>, Ping Zhu<sup>1</sup>, Minghai Liu<sup>1</sup>, Shaoxiang Ma<sup>1</sup>, Yong Yang<sup>1</sup>, Chuan Li<sup>1</sup>, Zhijiang Wang<sup>1</sup>, Ming Zhang<sup>1</sup>, Kexun Yu<sup>1</sup>, Xiwei Hu<sup>1</sup>, Y. Liang<sup>1,5</sup>, Q. Yu<sup>6</sup>, K. W. Gentle<sup>7</sup>, Yuan Pan<sup>1</sup> and the J-TEXT Team

- <sup>1</sup> International Joint Research Laboratory of Magnetic Confinement Fusion and Plasma Physics (IFPP), Huazhong University of Science and Technology, Wuhan, China
- <sup>2</sup> Southwestern Institute of Physics, Chengdu, China
- <sup>3</sup> Guizhou University of Commerce, Computer and information engineering college, Guiyang, China
- <sup>4</sup> ITER Organization
- <sup>5</sup> Forschungszentrum Jülich GmbH, IEK-Plasmaphysik, Jülich, Germany
- <sup>6</sup> Max-Planck-Institut für Plasmaphysik, Garching, Germany
- <sup>7</sup> Institute of Fusion Studies, University of Texas at Austin, Austin, United States of America Email: wangnc@hust.edu.cn; yhding@hust.edu.cn

#### **Abstract**

Recent research on the J-TEXT tokamak has significantly advanced the physics and control of high-temperature plasmas, directly supporting ITER and future reactor designs. Key upgrades include a new ICRF system (400 kW) and an enhanced ECRH system (1 MW), which have expanded capabilities for studying plasma heating and stability. The development of advanced 3D magnetic coil systems—DRMP, ID, and ERT coils—has enabled novel investigations into MHD instabilities, disruptions, and transport. A major finding is the NTM-triggered formation of eITBs, where magnetic islands nonlinearly interact with turbulence to suppress transport and steepen core temperature gradients. Furthermore, IKM-driven NTV torque has been identified as a key mechanism governing intrinsic rotation, with experiments confirming its densitydependent scaling. The application of ERT coils successfully created a Tokamak-Stellarator hybrid configuration, demonstrating nearly complete suppression of NTMs and a 20% increase in stable plasma current. For boundary control, the island divertor configuration reduced peak heat loads by ~50% and enabled detachment through SMBI fueling. Disruption mitigation experiments showed that low-n magnetic perturbations (e.g., 1/1, 2/2 modes) are most effective at suppressing runaway electrons, while the phase of locked islands directly impacts radiation asymmetry during MGI/SPI. AI-driven disruption prediction frameworks, incorporating adaptive anomaly detection and cross-machine domain adaptation (e.g., CORAL), have been developed to enhance forecast reliability with limited data. Interpretability analyses (e.g., SHAP) link model predictions to physical mechanisms, providing insights into disruption pathways. These collective advances in heating, 3D field control, stability, and AI forecasting provide critical solutions for managing plasma confinement and mitigating disruptions in future reactors.

#### 1. INTRODUCTION

As of a long-term research program, the J-TEXT [1, 2] experiments aim to develop fundamental physics and control mechanisms of high temperature tokamak plasma confinement and stability in support of the success operation of ITER and the design of future Chinese fusion reactor. Recent research has highlighted the significance of the role that non-axisymmetric magnetic perturbations, so called 3D magnetic perturbation (MP) fields, play in fundamentally 2D concept, i.e. tokamak. In this paper, the J-TEXT results achieved over the last two years, especially on the improved confinement with ECRH, 3D optimization for tokamak configuration, control of MHD instabilities, and plasma disruptions prediction, will be presented.

# 1.1. Upgrades or development of ICRF/ECRH

Ion Cyclotron Resonance Heating (ICRH) and Electron Cyclotron Resonance Heating (ECRH) are important auxiliary heating methods that are widely applied in magnetic confinement fusion experiments, as they are essential for elevating plasma temperature and enhancing confinement performance. These systems provide the necessary conditions for a variety of advanced physics studies and broaden plasma parameters. In recent years, the J-TEXT tokamak has undergone continuous upgrades to auxiliary heating systems, which has significantly increased its experimental capabilities and enabled the exploration of higher performance plasma states.

A new ICRF system has been developed for the J-TEXT tokamak since 2024. This system operates at frequencies between 20 and 35 MHz and is able to deliver up to 400 kW of power with a duration of one second, consisting

of two independent subsystems. The schematic diagram and the photographs of the subsystems are shown in FIG. 1, respectively. The system includes radio frequency generators, transmission lines, antennas, and a range of diagnostic probes for monitoring and evaluation. During the commissioning process, the system was shown to provide stable power at the intended frequencies, and diagnostic tools such as high-frequency magnetic probes, electrostatic probes, and voltage and current sensors were used to evaluate the coupling efficiency. The initial results confirmed that the system could possibly transfer energy to the plasma and performs reliably.

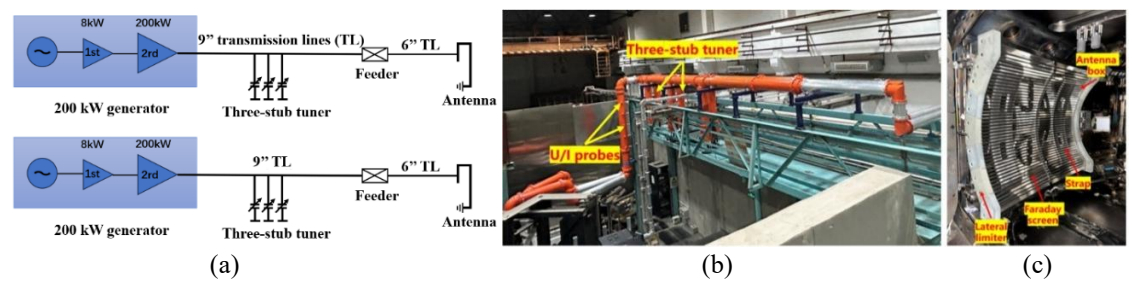


FIG. 1. Photographs of the J-TEXT ICRF system: (a) Schematic diagram; (b) transmission lines; (c) antennas.

# 1.2. Development of 3D magnetic field coil system

To advance the understanding of the impact of 3D magnetic fields on MHD instabilities, plasma disruptions, and turbulent transport, as well as to explore 3D magnetic configuration, J-TEXT has developed and installed several 3D field coil systems [3] in recent years, as summarized in FIG. 2. The double-turn DRMP coil system [4] (shown in blue) is designed to increase the field strength and control flexibility of the toroidal phases. In combination with

the pre-existing DRMP coils, about 6 Gs kA<sup>-1</sup> for m/n = 2/1RMP can be obtained. Island divertor (ID) coils [5, 6] (shown in yellow) consists of six sets, and is installed outside the vacuum vessel. The ID coil system is designed to generate magnetic divertor configuration, island enabling studies on divertor heat and particle exhaust as well as the mitigation of target plate heat loads. External rotational transform (ERT) coil system [7], consisting of two helical coils installed inside the vacuum vessel, is employed to investigate plasma Tokamakperformance in Stellarator hybrid configuration.

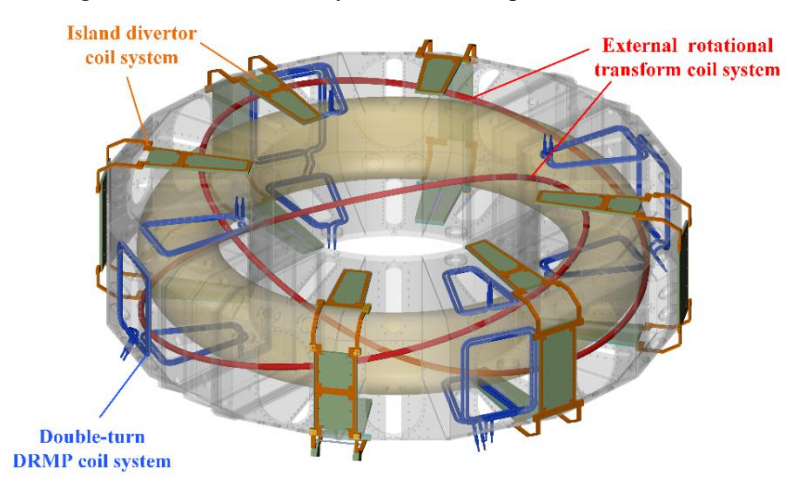


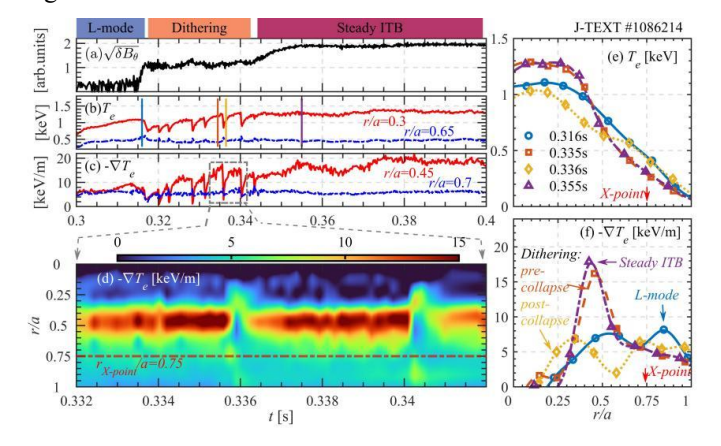
FIG. 2. Layout of Double-turn DRMP coil system (blue), Island divertor coil system (yellow) and External rotational transform coil system (red).

# 2. CORE CONFINEMENTS UNDER 3D FIELDS

#### 2.1. Impact of magnetic island on internal transport barrier

Electron thermal transport is a critical factor in magnetic confinement fusion, as fusion-born alpha particles primarily heat electrons in a reactor. For the first time, the increase of neoclassical tearing mode (NTM) amplitude has been observed to induce the reduction of the core electron thermal transport with the formation of an electron internal transport barrier (ITB) in the ECRH plasma on J-TEXT [8]. FIG. 3 displays a typical discharge with the NTM island triggering the ITB. The 400 kW ECRH was injected into the plasma core from 0.3 s. An NTM island was excited and started growing with the rotating frequency of  $\sim$ 5 kHz from 0.315 s. At small NTM amplitude, the profiles of  $T_{\rm e}$  and  $\nabla_r T_{\rm e}$  kept in L-mode structure, shown as the blue curves in FIG. 3(e) and (f). At medium NTM amplitude, the ITB is formed with a dithering phase, i.e. plasma transitions from no transport barrier to ITB or vice versa quasi-periodically. With NTM amplitude further increasing, the dithering ITB transitions into a steady ITB. The electron temperature gradient inside ITB increases with NTM amplitude. The trigger of ITB and further enhancement of ITB performance are also demonstrated by locking the island via applying a RMP field. The confinement energy with improved ITB can recover to the level prior to the appearance of the magnetic

islands. The reduction of density fluctuations in ITB region is observed and indicates the turbulence suppression during ITB formation.



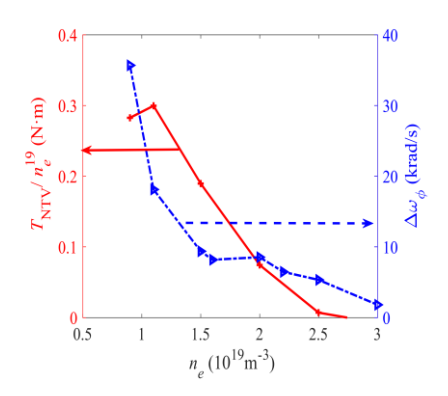


FIG. 3. Transition from L-mode to ITB revealed by the time evolution of (a) rotating island width, (b)  $T_e$  and (c)  $-\nabla_t T_e$  in discharge #1086214. (d) Time evolution of  $-\nabla_t T_e$  radial profile. (e)  $T_e$  and (f)  $-\nabla_t T_e$  profiles at 0.316s (L-mode), 0.335s (dithering pre-collapse), 0.336s (dithering post-collapse) and 0.355s (steady ITB). [8]

FIG. 4. The dependence of the normalization NTV torque from simulation and the change of toroidal rotation from J-TEXT experiment on plasma density.

A novel theoretical model is proposed for the NTM-triggered eITB formation, based on the nonlinear interaction between NTM and collisionless trapped electron mode (CTEM) turbulence. In this model, magnetic island-induced deformation enhances the precessional drift of trapped electrons, thereby stabilizing CTEM turbulence [9]. The resulting suppression of turbulence steepens the electron temperature gradient, which further destabilizes the NTM and amplifies magnetic deformation—forming a positive feedback loop that drives the eITB formation. In addition to the CTEM turbulence, the 3D field can also affect the toroidal ion temperature gradient (ITG) mode [10], whose suppression is critical for ion ITB formation. These experimental and theoretical results offer new insights for understanding ITB formation in thermal transport channel and robust ITB control with a 3D field.

#### 2.2. Impact of internal MHD mode on core momentum transport

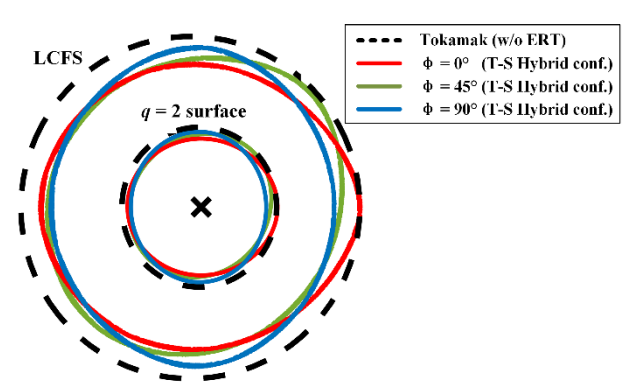
In previous work, a new model based on neoclassical toroidal viscosity (NTV) theory to understand intrinsic rotation have been proposed [11, 12]. The experimentally observed intrinsic toroidal rotation reversal and hysteresis have been well reproduced by momentum transport simulation using NTV torque driven by internal kink mode (IKM) modeled by NTVTOK [11], and the scaling law of threshold density for toroidal rotation reversal has also been studied [12]. To validate this proposed mechanism of MHD-induced NTV effects on intrinsic rotation, the experiments were conducted on the J-TEXT tokamak, employing ECRH to actively control IKM amplitude and investigate its influence on rotation damping [13]. The results demonstrate that on-axis ECRH strongly enhances the IKM, leading to a significant reduction in counter-current toroidal rotation. And the rotation change decreases with increasing plasma density, consistent with the observed reduction in IKM amplitude. These experimental findings provide direct validation for the previously proposed model of intrinsic rotation driven by IKM-induced NTV torque.

The modelling results from the NTVTOK code confirm that the IKM generates a positive NTV torque that drives rotation toward the co-current direction. As shown in FIG. 4, the density dependence of the normalized NTV torque from simulations (red solid line with stars) shows excellent agreement with the experimentally observed changes in toroidal rotation (blue dot-dash line with triangles), particularly in the medium to high density range. This comparison provides strong validation that the IKM-driven NTV torque serves as the primary mechanism behind the observed intrinsic rotation changes in ECRH plasmas. The work demonstrates that NTV torque, proportional to the square of the magnetic surface displacement caused by the IKM, effectively modifies core toroidal rotation. These findings provide direct evidence linking IKM amplitude to intrinsic rotation changes and underscore the importance of NTV effects in predicting and controlling rotation in future tokamak reactors.

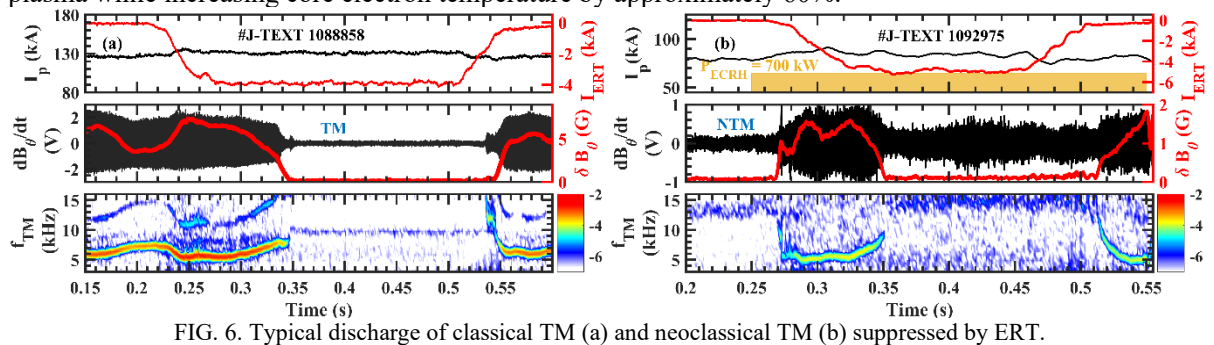
#### 2.3. Explore Tokamak-Stellarator hybrid configuration by applying external rotation transform

To explore innovative approaches for optimizing tokamak configurations and combining the advantages of both tokamaks and stellarators, a 3D ERT coil system has been installed on J-TEXT [7]. The designed dominant mode of the ERT coil is m/n = -2/2, while this non-resonant mode is chosen to prevent disruption due to the penetration of resonant components. Simulation results indicate that applying the ERT coil field leads to non-axisymmetric plasma shapes (as shown in FIG. 5), modifies the safety factor profile (or rotational transform in stellarator terminology), displaces rational surfaces, reduces the local current density gradient, and improves plasma stability. In standard J-TEXT discharge, the ERT coil can induce an external rotation transform  $t_{\text{vac}}/t_0 \sim 0.1$  at the plasma edge.

FIG. 5. Magnetic flux surface calculated by HINT. The red, green and blue solid lines represent the magnetic surfaces in the Tokamak-Stellarator hybrid configuration at  $\Phi=0^{\circ},\,45^{\circ},\,$  and  $90^{\circ},\,$  respectively. Black dashed lines represent the toroidal symmetric magnetic surfaces of the tokamak configuration without ERT for comparison. The plasma exhibits toroidal asymmetry after the application of ERT, thereby forming a 3D configuration distinct from the toroidal symmetric tokamak equilibrium.



The ERT coil system has been successfully applied to the J-TEXT plasma, experimentally realizing a Tokamak-Stellarator hybrid configurations [14]. Several promising experimental results have been observed. The MHD stability of T-S hybrid configuration plasmas is significantly enhanced [15]. Experimental results demonstrate that the application of ERT can effectively suppress both classical and neoclassical tearing modes, achieving nearly 100% suppression of NTMs and 70% suppression of TMs. FIG. 6 shows the Typical discharge of classical TM and NTM suppressed by ERT. Furthermore, a distinct evolution process, different from that driven by conventional RMP, has been observed: as the TM amplitude decreases, its frequency increases, while the field penetration or mode locking induced by resonant magnetic perturbation (RMP) fields are effectively avoided. Meanwhile, the T-S hybrid configuration enables an expanded operational range, with the maximum stable plasma current increased by approximately 20%. The T-S hybrid configuration enhances the parameters of plasma. ERT influences key plasma properties, including electron temperature and density. In electron ITB experiments, the ERT system achieves a stable NTM-free ITB plasma while increasing core electron temperature by approximately 60%.



# 3. DEVELOPMENT OF ISLAND DIVERTOR CONFIGURATION

The three-dimensional island divertor configuration has been successfully implemented on J-TEXT, so as to address the heat exhaust and impurity control in tokamak. The magnetic island was generated by applying externally RMP fields, while the intersection between the edge island and the divertor target was controlled by adjusting the edge safety factor  $q_a$ , thereby establishing the island divertor configuration [6–16, 17]. During the formation of the island divertor, overall plasma confinement was maintained despite the reduction in edge confinement volume due to the presence of the island. Compared with the standard poloidal divertor, the island divertor configuration exhibited a weaker dependence of power decay length on plasma current and a longer connection length, leading to a broader heat load distribution. Experimental results demonstrated that the peak heat load on the divertor target was reduced by approximately 50%, while the parallel heat flux fall-off length in the scrape-off layer (SOL) increased to 15.8~17.2 mm [18]. Furthermore, the impact of hydrogen fueling via

supersonic molecular beam injection (SMBI) on divertor heat flux distribution was investigated [19]. It was observed that power detachment occurred when the radiation front approached the last closed flux surface following each SMBI pulse. In addition to heat exhaust enhancement, the island divertor configuration was found to modulate impurity radiation around the X-point of the magnetic island, which could potentially improve the stability and control of radiative divertor operation. Moreover, the island divertor exhibited promising potential for enhancing impurity screening effects. Additionally, two types of edge island instabilities were identified during divertor experiments on J-TEXT. The first, self-sustained divertor oscillations, were attributed to a sequential transition between magnetic field penetration and screening states. The second, island-healing effects, were

induced by high-power ECRH [20]. These findings underscore the potential of the island divertor configuration as an effective strategy for improving heat exhaust and impurity control in tokamak operations. In the following, some key characteristics of the J-TEXT island divertor are presented.

## 3.1 Establishment of the island divertor configuration on J-TEXT

Island divertor experiments have been carried out on J-TEXT. FIG. 7 shows a representative discharge with a 4/1 island divertor with  $q_a > 4$  [6]. Field penetration occurs at t = 0.25s. During  $t = 0.25 \sim 0.42$ s, the ion saturation current exhibits two split strike points, confirming the island divertor formation. At t = 0.43s, the plasma reverts to the limiter as the RMP current is switched off. During the island divertor phase, as shown in FIG. 7 (f), the divertor heat load is reduced by up to 50%, from  $\sim 0.8$  to  $\sim 0.4$   $MW \cdot m^{-2}$  compared with the limiter phase. Moreover, as indicated in FIG. 8, the edge CIII radiation undergoes significant modifications after configuration transition. The island divertor reveals strong changes in edge CIII radiation, showing clear 3D structures such as X point like and divertor leg like patterns.

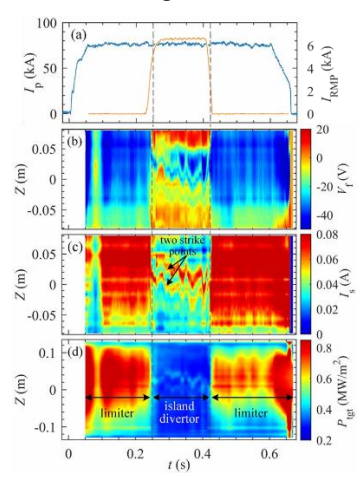


FIG. 7 Overview of main plasma parameters for the experimental discharge #1089496 on J-TEXT.

showing clear 3D structures such as X-point-like and divertor-leg-like patterns.

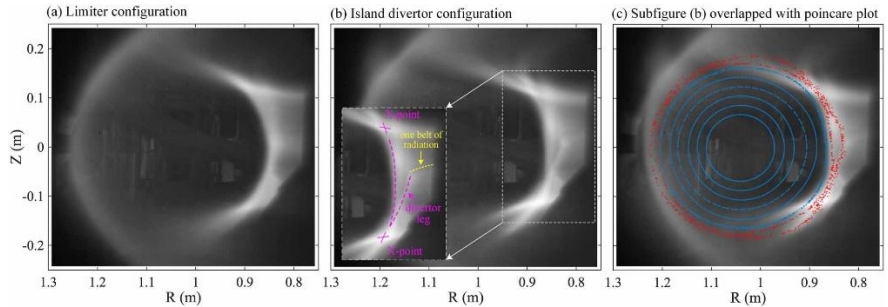


FIG. 8. The CIII impurity radiation distribution for the experiment discharge #1087724 on J-TEXT

# 3.2 Detachment of the island divertor configuration

For future devices, detachment is a key challenge for all divertor concepts. Therefore, it is necessary to investigate detachment and its characteristics in the island divertor. On J-TEXT, thermal detachment has been achieved using SMBI hydrogen fueling [19]. Scanning the SMBI pulse width shows that detachment requires fueling amount above  $0.494 \times 10^{19}$ . Additionally, as shown in FIG. 10, radiation measurements show that when the radiation front reaches the LCFS, the peak target heat load can drop to its minimum.

# 3.3 Characteristics of plasma parameters with different edge 3D magnetic topology

The SOL structure in the island divertor can be tuned by adjusting  $q_a$  and the applied RMPs. Therefore, it is necessary to link the edge plasma profiles and the edge 3D magnetic topology. Langmuir probe and RFA are develop to measure edge parameters [18, 21, 22]. FIG. 9 presents the distribution of edge connection length  $(L_c)$ , electron temperature  $T_e$ , radial electric field  $E_r$  and electron pressure  $P_e$  under different configurations. Flat  $P_e$  is observed inside edge-closed and SOL remnant islands (FIG. 9 (d) and (e)). During the transition from closed to partially opened islands, the local flat  $P_e$  region shifts outward and narrow.  $E_r$  exhibits a negative well

inside the remnant island with infinite  $L_c$  and in the SOL regions where  $L_c \gg \lambda_e$  (electron mean free path), but becomes positive in the SOL regions where  $L_c$  is relatively short.

In addition to electron distribution characteristics, the ion temperature  $(T_i)$  and the ion-to-electron temperature ratio  $(\tau_{i/e})$  are measured using the RFA. The  $\tau_{i/e}$  decrease as ion self-collisionality  $(v_{SOL}^*)$  increase. However, it is obvious the  $\tau_{i/e}$  dependence on  $v_{SOL}^*$  is different under different edge magnetic topology.

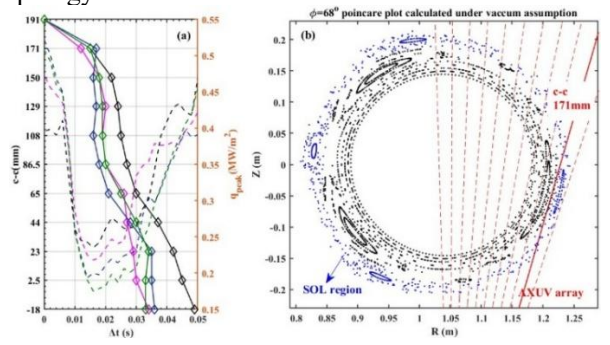


FIG. 10. Time evolutions of peak heat flux and radiation front during each SMBI pulse period.

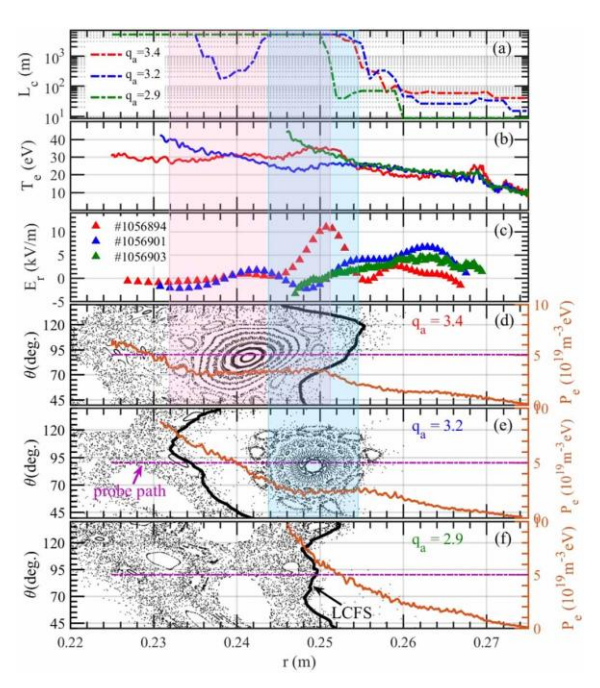


FIG. 9. Radial profiles for different  $q_a$  cases

# 3.4 Instability of the island divertor

The operation of the island divertor configuration is closely tied to the stability of the edge island. Once there is a change in the width and phase of the edge island, this may lead to the deposition of heat load outside the divertor targets. Therefore, the stability of the edge island is of great concern in the experiment.

Two types of edge island instabilities were identified during divertor experiments on J-TEXT. The first, self-sustained divertor oscillations, is attributed to a sequential transition between magnetic field penetration and screening states [23]. This drive periodical outward flow of particles and heat through the X-point of the edge magnetic island, like periodic ELMs collapse. The second effect, island healing, is induced by high-power ECRH [24]. When the ECRH power exceeds a threshold—strongly dependent on the deposition location—the edge open island shrinks significantly. Both effects strongly impact the stable operation of the island divertor.

The secondary MHD instability, so called m-BAE, is also modified by the island divertor. In the course of the 3/1 island divertor configuration scan, an m-BAE is observed to be localized within the isolated helical flux tube associated with the edge 3/1 island. The m-BAE forms a standing wave inside the magnetic island, with its nodes located at the X- and O-points of the magnetic island. When the island is cut open by target plates during  $q_a$  scan, the m-BAE is found to remain inside the remnant closed island in the SOL, but its amplitude decreases as the width of the remnant island becomes smaller.

# 3.5 3D equilibrium reconstruction and heat load prediction – for design and optimization

Plasma response to RMPs is crucial for island divertor design and operation. On J-TEXT, the penetration threshold and 3D equilibrium are studied using HINT and MARS-F [25]. Based on the predicted equilibrium, the FusionSC field-line diffusion model [26] is applied to estimate divertor heat loads. Experimental and simulation results agree well (FIG. 11), showing that accounting for island screening yields more reliable equilibrium. This lays the basis for 3D magnetic equilibrium design and heat-load optimization.

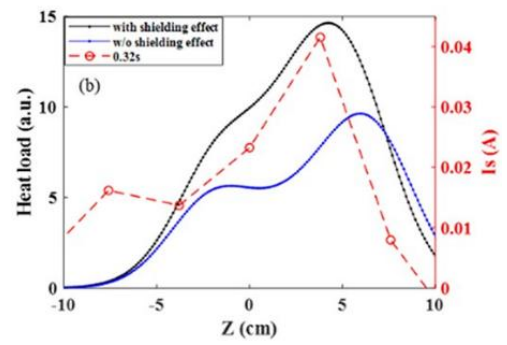


FIG. 11. The predicted heat flux with/without shielding effect without shielding effect and the distribution of the ion saturation current on divertor target. [25]

#### 4. DISRUPTION PHYSICS AND CONTROL

#### 4.1. Disruption avoidance by RMP and ECRH

Stabilization of the tearing modes (TM) and locked modes (LM) are of great importance for the tokamak plasma operation. The rotating 2/1 TM can be completely suppressed by 230 kW ECRH deposited close to the rational surface [27]. The ECW deposition location in the plasma can be changed by varying the poloidal angle of the steering mirror. It is found that the suppression is more effective when the ECW power is deposited closer to the rational surface. The m/n = 2/1 TM can only be partially suppressed when the ECW power below approximately 200 kW. The island width is decreased and will be stabilized at a saturated width.

The ECRH power required for LM island suppression can be reduced to 100 kW when the island's O-point is aligned with the ECRH deposition position by applying RMP to control the phase of the 2/1 TM, and disruption avoidance by the suppression of the 2/1 LM using ECRH has been achieved [28]. Local heating at the island's O-point and the resulting temperature perturbations play a dominant role in mode suppression. The temperature perturbations within the magnetic island, measured by electron cyclotron emission imaging (ECEI) with high temporal and spatial resolution during mode-locking state. Figure 10(a) and (b) correspond the case of LM island suppression. In figure 10(a), the island's O-point temperature increases from 0.104 keV to 0.278 keV over 12 ms, resulting in a temperature rise of 0.174 keV after 100 kW of ECW is applied. Simultaneously, the  $\delta B_{\theta}$  decreases from 12 Gs to 5 Gs, indicating effective suppression of the LM island. For rotating island suppression, the temperature of the O-point is obtained from the small speaks in the ECEI signal, as shown in figure XX(f). The temperature gradually increases with a remaining sinusoidal component indicating only partial suppression of the mode. The temperature of the O-point rises from 0.136 keV to 0.224 keV. The results indicate that continuous heating at the island's O-point produces greater temperature perturbations than heating a rotating island. Thus, the LM suppression strategy can improve the efficiency of island suppression by ECW, reducing the power needed for mode suppression.

Furthermore, the effect of misalignment between the island's O-point and the ECW deposition region on mode suppression has been investigated by adjusting the RMP phase. Figure 11 shows the time evolution of the mode amplitude when the mode is locked at four different LM phases. The most effective LM suppression occurs when ECW power is accurately aligned with the island's O-point, resulting in successful disruption avoidance. For the  $\xi_0 = 292^\circ$ , where the ECW power is deposited at the island's O-point, the mode is completely suppressed after the mode-locking occurs. The mode cannot be suppressed by ECRH when the island's X-point is aligned with the ECW deposition position, shown in figure 11(a). This scenario may lead to earlier disruption compared to cases without ECW.

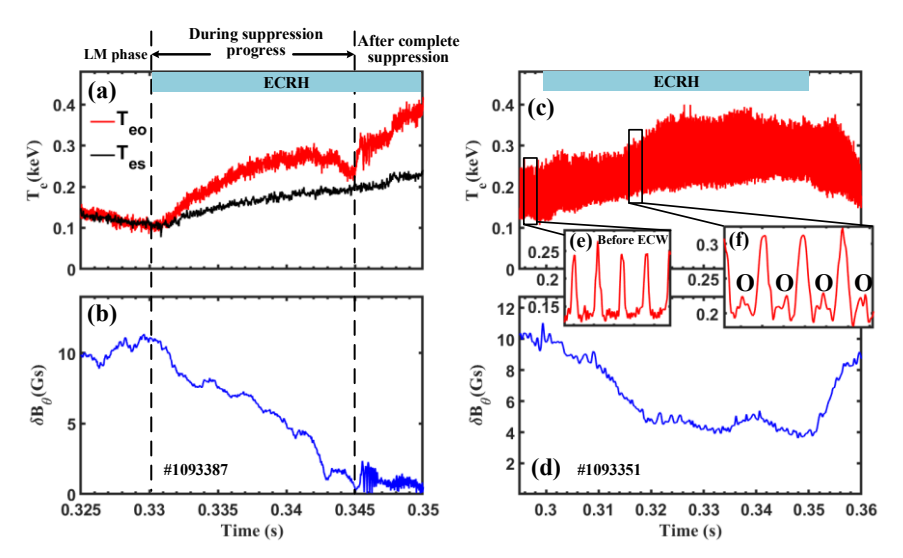


FIG. 12. The time evolution of the island's O-point temperature measured by ECEI and the LM amplitude  $\delta B_{\theta}$  for the LM island and the rotating mode suppression scheme, respectively. (a) and (b) correspond to the case of LM suppression in discharge #1093387. (c) and (d) correspond to the case of RM suppression in discharge #1093351. (e) and (f) show the detailed ECEI signals corresponding to the period marked by the solid line in (c), before and after ECW application, respectively. The ECW power in the two discharges is the same as 100 kW. The same ECEI channel is selected to measure the temperature of the O-point.

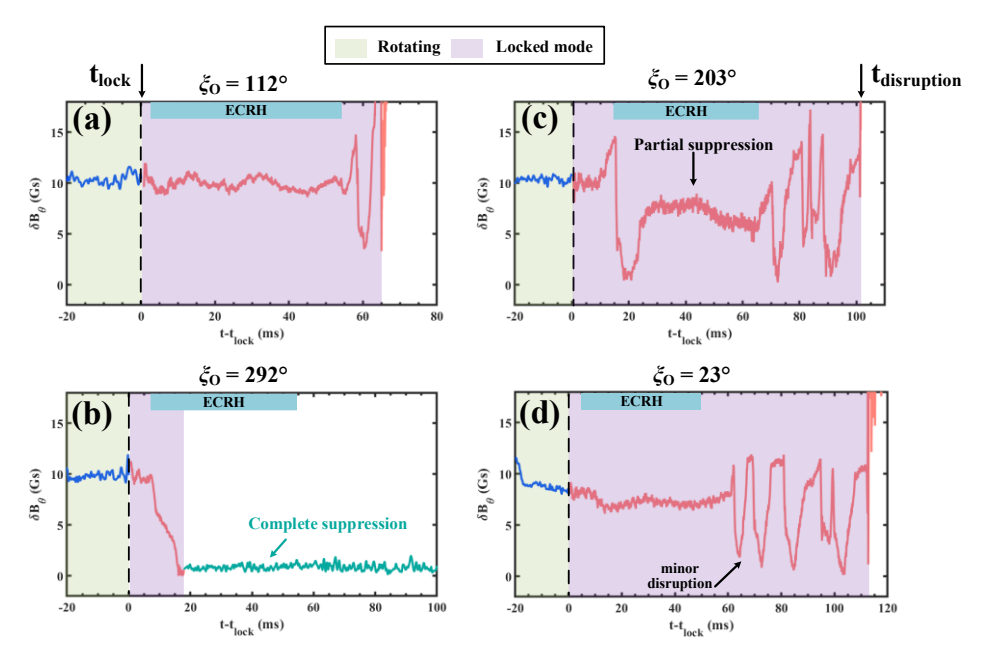


FIG. 13. Time traces of the mode amplitude for four island's O-point phases. With  $\xi_0 = 112^\circ$ ,  $203^\circ$ ,  $292^\circ$  and  $23^\circ$ , panels (a), (b), (c) and (d), respectively. The time t = 0 represents the time of the mode-locking, marked by vertical dotted lines. The case of  $\xi_0 = 292^\circ$  corresponds that the island's O-point is aligned with the ECRH deposition position.

#### 4.2. Disruption mitigation tools (EMPI etc)

During the operation of the tokamak device, plasma disruptions can lead to problems such as thermal loads, electromagnetic forces, and runaway currents, which pose a severe threat to device safety. Currently, mainstream disruption mitigation methods like Massive Gas Injection (MGI) and Shattered Pellet Injection (SPI) suffer from limitations including restricted impurity injection speeds and inability to meet the demands of short warning times. In contrast, the electromagnetic injection method, characterized by its high-speed response, has emerged as a promising alternative. Based on this, the J-TEXT team has developed the Electromagnetic Pellet Injection (EMPI) system.

### 4.3.1 EMPI

The EMPI system is mainly developed based on the principle of electromagnetic railguns, consisting of a 1.5-meter acceleration section and a 1.5 meter deceleration section (FIG. 14) [29]. It adopts an X-type armature (10 g) to achieve separation between the armature and the pellet, with a maximum pellet velocity of up to 1000 m/s. However, it has several drawbacks: lack of an armature recovery device, severe rail ablation, muzzle arcing lasting more than 15 ms, high risk of metallic impurity contamination, and it has not been integrated into the tokamak device for operation. Further optimization is urgently required.

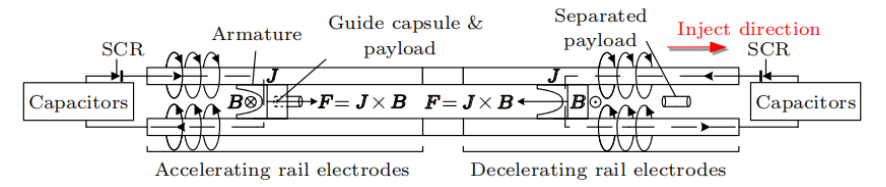


FIG. 14 EMPI configuration.

#### 4.3.2 Optimization of EMPI

To address the existing issues of the EMPI system, technical optimizations have been carried out. A vacuum system and a curved recovery rail have been added to the previous configuration, and an augmented rail design has been adopted (FIG. 15). During the operation of the EMPI, arcing is prone to occur at the contact between the rail and the armature as well as at the muzzle, leading to rail ablation and generation of metallic impurities, which affect the disruption mitigation effect and device lifespan [30]. The J-TEXT team has developed a hybrid arc suppression system, and through parameter optimization, the arc energy has been reduced by more than 90%. Aiming at the problems of current concentration and intensified ablation caused by poor rail-armature contact, convex/concave coupling structures based on the X-type armature have been proposed. Through COMSOL multiphysics simulation and experimental verification, the concave structure has shown the optimal performance in reducing ablation, optimizing electrical contact, and improving launch efficiency [31]. To achieve precise velocity control of impurity pellets (e.g., 800 m/s, 1000 m/s, 1200 m/s) under different disruption scenarios, a genetic

algorithm-based pulse power supply timing optimization method has been developed [32]. By controlling the discharge current waveform, the armature moves uniformly and linearly, enabling precise control of the pellet velocity [33]. At present, the EMPI system still has certain issues that need to be resolved.

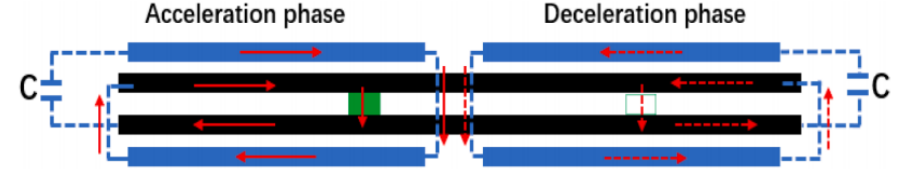


FIG. 15. Augmented type rail. The inner rail gap is 10mm, the gap between the inner and outer rails is 5mm. The rail height is 10mm. C is a capacitor, and the capacitance used in the experiment is 4.1 mF. The red solid arrow indicates the direction of the current during the acceleration phase, and the red dotted arrow indicates the direction of the current during the deceleration phase. The blue rail is the augmented rail.

#### 4.3. Disruption mitigation experiments

Plasma disruption in tokamak devices is a critical challenge limiting the practical application of nuclear fusion energy. Runaway Electrons (REs) generated during disruptions can severely damage the device's first wall, while radiation asymmetry causes excessive local heat loads, endangering device safety. To address the above issues, a series of disruption mitigation experiments have been conducted based on the J-TEXT tokamak device. The core objectives include verifying the suppression effect of different magnetic perturbation modes on runaway electrons, revealing the regulation mechanism of the 2/1 tearing mode on radiation asymmetry, and optimizing disruption mitigation strategies to reduce disruption hazards, thereby providing experimental basis and data support for disruption control in next-generation large-scale tokamaks (such as ITER).

# 4.4.1 Experiments on Runaway Electron Suppression

By reversing the plasma current, the ERT coils produced vacuum magnetic fields in 1/1, 2/2, 3/3, and 4/4 modes. [34] Argon (Ar) impurity gas was injected at a fixed rate to trigger plasma disruption. Results showed that low-n modes (1/1, 2/2) were much better at suppressing runaway electrons than high-n modes (3/3, 4/4) (FIG. 16). This is because low-n modes make the magnetic surface more stochastic and shorten the connection length of magnetic field lines. Among these modes, the 1/1 mode coil could fully suppress the runaway current at specific helical phases, and the proportion of confined runaway electrons showed a sinusoidal relationship with the coil phase. Physically, passive magnetic perturbations accelerated magnetic surface stochasticity by increasing magnetic perturbation energy (especially the n=1 component), making the runaway electron loss rate exceed the

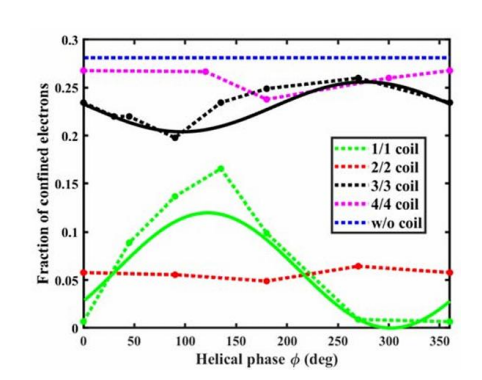


FIG. 16. The fraction of confined electrons of the passive field in different helical phases.

generation rate and thus suppressing the formation of the runaway current plateau.

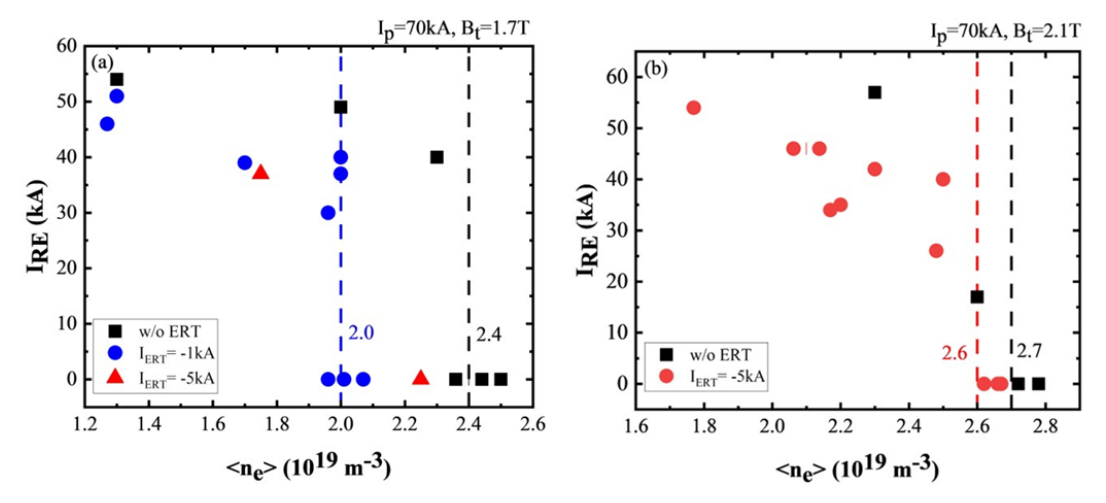


FIG. 17. Dependence of the runaway current and electron densities with different 3D helical fields: (a)  $B_t = 1.7 \text{ T}$  and (b)  $B_t = 2.1 \text{ T}$ .

For the experiment on suppressing runaway electrons and regulating density thresholds via 3D helical magnetic perturbation, ERT helical coils generated two magnetic perturbation modes by changing the coil current direction: co-current mode and counter-current mode. Fast MGI injection of argon gas triggered a stable runaway current. The results showed that the counter-current mode could shift the plasma to the High-Field Side (HFS), enhance

high-frequency magnetic fluctuations to accelerate radial loss of runaway electrons, shorten disruption cooling time (including prethermal quench (pre-TQ) and thermal quench (TQ) phases), and increase the population of high-energy electron tails. The interaction between these tails and high-frequency fluctuations further suppressed runaway electrons [35]. In contrast, the cocurrent mode only slightly enhanced magnetic fluctuations on the Low-Field Side (LFS), resulting in a weak suppression effect (

). In terms of electron density threshold regulation: without magnetic perturbation, the runaway electron suppression threshold at  $1.7~\mathrm{T}$  was  $2.4\times10^{19}\mathrm{m}^{-3}$ , which decreased to  $2.0\times10^{19}\mathrm{m}^{-3}$  after applying counter-MPs (I\_{ERT}=-1kA). At  $2.1~\mathrm{T}$ , the threshold decreased from  $2.7\times10^{19}\mathrm{m}^{-3}$  to  $2.6\times10^{19}\mathrm{m}^{-3}$ . Magnetic perturbation effects were more significant under low toroidal magnetic fields, confirming that counter-MPs could reduce the electron density threshold required for runaway electron suppression by enhancing magnetic fluctuations, thereby decreasing the demand for MGI impurity injection.

# 4.4.2 Experiments on Radiation Asymmetry Control

The experiments of radiation asymmetry on J-TEXT tokamak have been conducted. The results showed that in both MGI and SPI experiments, the Toroidal Peaking Factor (TPF) exhibited an approximately sinusoidal relationship with the phase of the 2/1 locked magnetic island. When the X-point of the magnetic island was aligned with the impurity injection position, the impurity injection depth was greater, leading to concentrated radiation and the maximum TPF. In contrast, when the injection position was between the X-point and O-point of the magnetic island, impurities were blocked by the magnetic island, enhancing toroidal transport and resulting in more uniform radiation, thus minimizing the TPF [36].

When comparing the performance of MGI and SPI, the average TPF of MGI was approximately 2.44, while that of SPI was around 1.93 (FIG. 18). SPI exhibited weaker radiation asymmetry, which was attributed to its deeper injection depth and more complete impurity assimilation. In terms of the goodness of sine fitting, MGI showed a more regular fit,

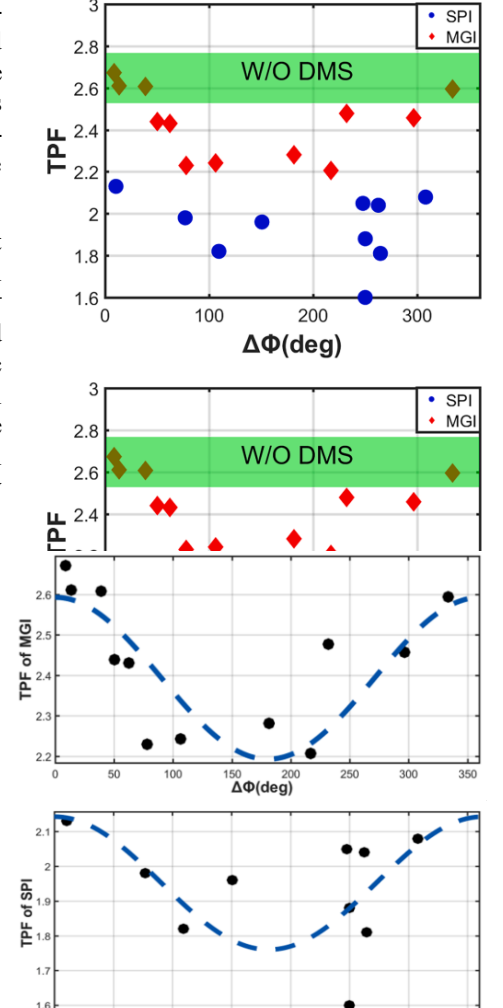


FIG. 19. Relationship between locked island phase and the TPF of MGI and SPI.

whereas SPI data were more scattered (FIG. 19). Additionally, the thermal quench (TQ) phase was the main stage of radiation asymmetry, while the current quench (CQ) phase had low radiation energy and a TPF close to 1, causing minimal harm to the device.

# 5. AI AND DISRUPTION PREDICTION

Significant efforts have been made in both the disruption prediction for future tokamak reactors [37] and the interpretability research [38]. The future tokamak reactors should be protected starting from the first discharge, therefore, an adaptive anomaly detection disruption prediction, which allowing the predictor to adapt to changes in the discharge scenario and maintain high prediction performance has been developed [39]. Cross-machine disruption prediction based on domain adaptation could aligned the data from source and target domain better to reach a better prediction performance than the model trained by mixing data [40]. Furthermore, the study examines how to achieve optimal performance by balancing data-driven and physics priors, using domain-invariant representation learning [41].

The interpretability analysis of the cross-tokamak disruption prediction shows that the model learned more consistent disruption-contributing features performed better in new tokamaks [6]. Otherwise, conflicting patterns can reduce the model performance, therefore, an instance-based transfer learning technique which trains the model

using a dataset generated with the strategy involves instance and feature selection based on interpretability analysis [42]. The interpretability analysis could also help researcher to decode the cause of disruption for further disruption mechanisms studies. In J-TEXT ECRH experiments, the interpretability analysis of disruption prediction model could determine whether the density limit has been reached [43]. To further investigate the causes of density limit disruptions, a disruption prediction with no Greenwald fraction features has also been trained to distinguish density limit disruption from the other disruptions to learn the real density limit physics.

# 5.1. Cross-machine disruption prediction

#### 5.1.1. Adaptive Anomaly Detection Disruption Prediction

In future high-performance tokamaks such as ITER, the plasma energy storage is extremely high. The disruption could cause severe damage to the device, making it impossible to collect sufficient disruption data to train supervised learning models. Moreover, protection must begin from the very first discharge on the new device. An adaptive anomaly detection predictor is pre-trained on existing devices and then updated after every shot on the new machine so it can operate immediately even when only non-disruptive data are available. To reduce the dependency on new device data during cross-tokamak transfer, the J-TEXT team designed an Enhanced Convolutional Autoencoder Anomaly Detection (E-CAAD) model. We also proposed a comprehensive strategy based on the E-CAAD predictor that enables disruption prediction from the first discharge on a new device and allow the predictor to automatically adapt to changes in plasma operation scenarios. This strategy continuously updates the anomaly detection threshold as discharges proceed, improving adaptation to the operation of a new device.

# 5.1.2. Cross-machine disruption prediction based on domain adaptation

To address data scarcity and domain shift between machines, we construct a physics-guided feature space from shared diagnostics and introduce domain adaptation (DA) with CORAL, extended to a supervised variant that aligns disruptive and non-disruptive classes separately, to match the source J-TEXT and target EAST data. With a small amount of target data, the AUC increases from about 0.64 in zero shot to about 0.76 with simple mixing,

about 0.80 with unsupervised CORAL, and about 0.89 with supervised CORAL, close to the target only upper bound of about 0.94. FIG. 20 presents the model structure and training pipeline that support these results, including feature extraction, alignment, classifier training, and the subsequent explainer.

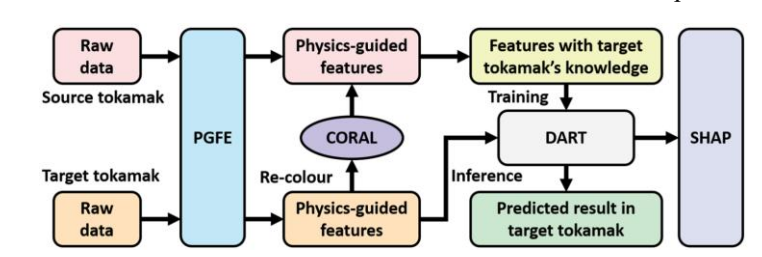


FIG. 20. The structure of the cross-tokamak disruption prediction based on DA.

# 5.1.3. Cross-machine Disruption Prediction via Domain- Invariant and Physics-Guided Representation Learning

To address the challenge of data scarcity in future fusion reactors, a physics-based domain adaptation framework PhyDANet is proposed. The framework integrates domain-invariant representation learning with physics-based output constraints and physics-guided feature reconstruction, as is shown in FIG. 21, enabling the transfer of knowledge from existing machines while exploiting predictions in established physical principles. Using J-TEXT as the existing tokamak and EAST as the target, the study demonstrated how the balance between physics priors and data-driven learning shifts across data regimes: physics priors dominate under scarce data, while domain adaptation and device-specific features become increasingly effective as more data accumulate. These results highlight a practical path toward reliable early-stage disruption prediction in next-generation fusion reactors such as ITER.

# 5.2. Interpretability

#### 5.2.1. Interpretability study in cross-machine disruption prediction

To build trust and diagnostic insight in cross machine transfer, interpretability is used to examine how domain adaptation shifts data distributions and which features drive predictions so that learned knowledge resembles what a model would learn with abundant target data. Intrinsic interpretability from physics guided feature engineering combined with CORAL is complemented by post hoc SHAP analysis on EAST that compares three transfer settings, namely naive mixing, unsupervised alignment, and supervised alignment, against an EAST full data benchmark. The SHAP analyses indicate that supervised alignment best reproduces target relevant global effects,

while unsupervised alignment provides a strong starting point when labels are scarce. The combination offers a principled way to diagnose transfer quality, select features that are stable across devices, and identify failure modes early enough to influence data collection and algorithm choice. Quantitative features include earth mover distance between source and target feature effects, calibration curves for probability outputs, and reliability diagrams that assess whether confidence aligns with observed frequencies. When divergence is detected, the workflow recommends collecting targeted examples in regions of mismatch and revisiting feature definitions to emphasize device independent signals. The approach provides a checklist that connects attribution to concrete data actions and helps decide when to re align, when to relabel, and when to change the model class. A comparison of the three methods shows that S-CORAL achieve the highest score of 7.

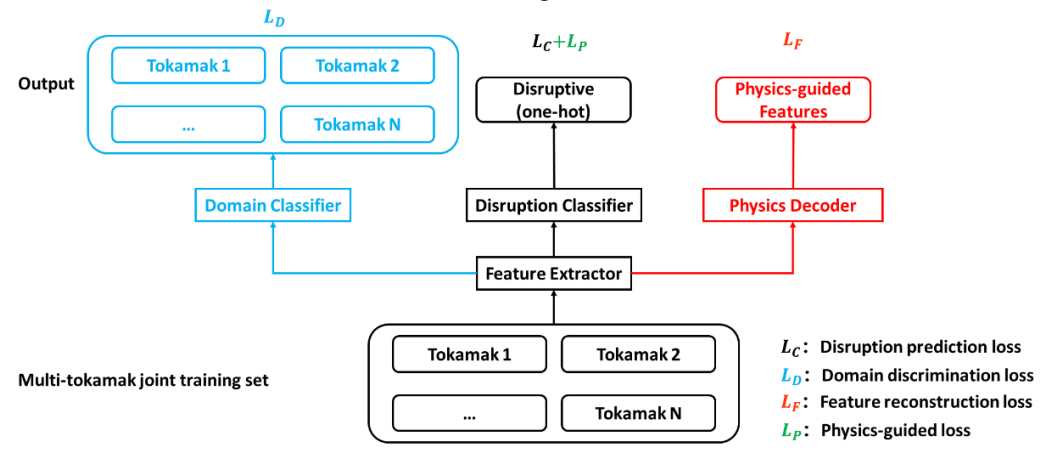


FIG. 21. The illustration of the physics-based domain adaptation framework (PhyDANet).

#### 5.2.2. Decoding causes from data-driven models based on the Interpretability study

This study investigates how ECRH influences high-density disruptions on J-TEXT and demonstrates that an interpretable, physics-guided prediction framework can disentangle superficially similar events with distinct causal pathways. A tree-based classifier is paired with SHAP attribution and physics-guided feature engineering to track the evolving contributions of core electron density, radiated power, Mirnov probe amplitudes, and weighted mode-number metrics. Case analyses show that, although disruptions during ECRH may occur at densities lower than canonical limits, their dominant drivers shift from density-limit progression to radiation- or MHD-triggered routes, with clear, time-resolved changes in feature importance preceding the terminal event. These results indicate that ECRH does not intrinsically lower the density limit but modifies the balance between radiation and MHD activity, thereby changing the route to disruption. By localizing which signals become predictive and when, the framework provides mechanistic guidance for targeted control and alarm logic, and it motivates future work to incorporate turbulence and MARFE-related descriptors to strengthen the physical interpretability of density-limit predictions.

# 6. SUMMARY AND OUTLOOK

Recent experimental advancements on the J-TEXT tokamak have demonstrated significant progress in understanding and controlling magnetically confined plasmas under 3D magnetic perturbations. Key hardware upgrades include enhanced ICRF (400 kW) and ECRH (1 MW) systems alongside sophisticated 3D coil systems (DRMP, ID, ERT), enabling unprecedented capabilities for manipulating plasma magnetic topology and stability. These developments have facilitated novel investigations into MHD instabilities, disruption dynamics, and transport phenomena, establishing J-TEXT as a unique platform for 3D plasma physics research relevant to next-generation fusion devices.

Substantial physics breakthroughs have been achieved in both core and boundary plasma behavior. Notably, NTM-triggered eITB formation has been observed and theoretically explained through nonlinear island-turbulence interactions, while IKM-driven NTV effects have been confirmed as the dominant mechanism governing intrinsic rotation dynamics. The pioneering Tokamak-Stellarator hybrid configuration achieved through ERT application demonstrated remarkable capabilities: nearly complete NTM suppression, 20% increased stable plasma current, and 60% higher core electron temperature. Concurrently, the implemented island

divertor configuration reduced peak heat loads by approximately 50% through optimized 3D magnetic topology, with successful detachment achieved via SMBI fueling.

These experimental achievements are complemented by advanced control and prediction methodologies. Disruption mitigation strategies have been refined through RMP+ECRH techniques that reduce suppression power requirements to 100 kW, while systematic studies identified low-n perturbations as most effective for RE suppression. Furthermore, machine learning frameworks employing domain adaptation techniques have enabled cross-machine disruption prediction with significantly improved performance, and interpretability analyses have validated the physical relevance of predictive features. Collectively, J-TEXT's research outcomes provide critical insights and solutions for managing plasma confinement, stability, and disruption risks in future fusion reactors, with direct implications for ITER operation and DEMO design.

#### **ACKNOWLEDGEMENTS**

This work is supported by the National MCF Energy R&D Program of China (Contract No. 2024YFE03060000, 2018YFE0309100, 2018YFE0310300, 2019YFE03010004, 2022YFE03040004), the National Natural Science Foundation of China (Nos. 12075096, 12047526, 12275098) and the Hubei International Science and Technology Cooperation Projects (No. 2022EHB003).

#### REFERENCES

- [1] Wang N. C. et al 2022 Nucl. Fusion 62 042016
- [2] Ding Y. et al 2024 Nucl. Fusion 64 112005
- [3] Jiang Z. H. et al 2022 Plasma Sci. Technol. 24 124014
- [4] Huang Z. et al 2023 Plasma Sci. Technol. 25115601
- [5] Zhou S. et al 2019 Fusion Eng. Des. 146 902
- [6] Zhou S. et al 2025 Nucl. Fusion 65 016020
- [7] Li Y. B. et al 2024 Fusion Eng. Des. 206 114591
- [8] Mao F. Y. et al 2025 Nucl. Fusion 65 066018
- [9] Huang Z. S. et al (to be submitted)
- [10] Huang Z. S. et al 2025 Nucl. Fusion 65 016021
- [11] Li H. H. et al 2021 Nucl. Fusion 61 104002
- [12] Li H. H. et al 2023 Phys. Plasmas 30 052504
- [13] Li H. H. et al 2025 Nucl. Fusion 61 104002
- [14] Li Y. B. et al 2024 50th EPS Conf. on Plasma Phys. P2.052
- [15] Li Y.B. AAPPS 2025
- [16] Liang Y. et al 2022 Plasma Sci. Technol. 24 124021
- [17] Liang Y., This conference, EX-D, #2781
- [18] Yang J. et al 2024 Nucl. Fusion 64 056030
- [19] Yang Y.T. et al 2024 Plasma Sci. Technol. 26 125102
- [20] Hou Z. R. *et al* 2025 Plasma Phys. Control. Fusion.
- [21] Yang J. et al 2024 Nucl. Fusion 64 024001
- [22] Li C. K. et al 2024 Plasma Sci. Technol. 26 025101.
- [23] Hua J. K., Nucl. Fusion, 2025 (submitted)
- [24] Hou Z. R. et al 2025 Plasma Phys. Control. Fusion 67 045025.
- [25] Xie W. *et al* Plasma Science and Technology, 2024, 26(11): 115104.

- [26] Knieps A. et al 2024 50th EPS Conf. on Plasma Phys.
- [27] Fang J. G. et al 2024 Plasma Sci. Technol. 26 085101
- [28] Fang J. G. et al 2025 Eur. Phys. J. Spec. Top. https://doi.org/10.1140/epjs/s11734-024-01461-3
- [29] Li F. et al 2023 Chinese Phys. B 32 075205
- [30] Yu Y.L. et al 2024 Fusion Eng. Des. 198 114100
- [31] Nie Z. et al 2024 IEEE Transactions on Plasma Science 52 3326
- [32] Nie Z. et al 2023 IEEE 4th China International Youth Conference On Electrical Engineering (CIYCEE)
- [33] Yu Y.L. et al 2024 Fusion Eng. Des. 208 114701
- [34] Li K. Z. et al 2023 IEEE 4th China International Youth Conference On Electrical Engineering (CIYCEE)
- [35] Yan W. et al 2025 Plasma Sci. Technol. 27 035104
- [36] Liu F.X. et al 2024 Fusion Eng. Des. 199 114152
- [37] Zheng W. This conference, EX-S, #3140
- [38] Shen C. This conference, EX-S, #3167
- [39] Ai X. K. et al 2024 Nuclear Engineering and Technology 56 4 1501-1512; 2024 Plasma Phys. Control. Fusion 66 085015; 2025 Nucl. Fusion 65 036011
- [40] Shen C. S. et al 2024 Nucl. Fusion 64 066036
- [41] Xue F. et al 2025 Nucl. Fusion submitted
- [42] Zhong Y. et al 2024 Nucl. Fusion 64 096012
- [43] Lin W. et al 2024 4th International Conference on Energy, Power and Electrical Engineering (EPEE)